

1     **CLIQ-BID: A method to quantify bacteria-induced damage to eukaryotic**  
2                     **cells by automated live-imaging of bright nuclei**

3     Yann Wallez<sup>1</sup>, Stéphanie Bouillot<sup>1</sup>, Emmanuelle Soleilhac<sup>2</sup>, Philippe Huber<sup>1</sup>, Ina Attrée<sup>1</sup> &  
4                                     Eric Faudry<sup>1\*</sup>

5     <sup>1</sup>UGA, CEA, INSERM, CNRS, Bacterial Pathogenesis and Cellular Responses, Biosciences  
6     and Biotechnology Institute of Grenoble, France. <sup>2</sup>UGA, CEA, INSERM; Genetics &  
7     Chemogenomics, CMBA Platform, Biosciences and Biotechnology Institute of Grenoble,  
8     France

9  
10    \* Correspondence and requests for materials should be addressed to E.F. (email:  
11    [eric.faudry@cea.fr](mailto:eric.faudry@cea.fr))

12

13 ABSTRACT

14 Pathogenic bacteria induce eukaryotic cell damage which range from discrete modifications  
15 of signalling pathways, to morphological alterations and even to cell death. Accurate  
16 quantitative detection of these events is necessary for studying host-pathogen interactions and  
17 for developing strategies to protect host organisms from bacterial infections. Investigation of  
18 morphological changes is cumbersome and not adapted to high-throughput and kinetics  
19 measurements. Here, we describe a simple and cost-effective method based on automated  
20 analysis of live cells with stained nuclei, which allows real-time quantification of bacteria-  
21 induced eukaryotic cell damage at single-cell resolution. We demonstrate that this automated  
22 high-throughput microscopy approach permits screening of libraries composed of  
23 interference-RNA, bacterial strains, antibodies and chemical compounds in *ex vivo* infection  
24 settings. The use of fluorescently-labelled bacteria enables the concomitant detection of  
25 changes in bacterial growth. Using this method named CLIQ-BID (Cell Live Imaging  
26 Quantification of Bacteria Induced Damage), we were able to distinguish the virulence  
27 profiles of different pathogenic bacterial species and clinical strains.

## 28 INTRODUCTION

29 Bacterial toxins targeting eukaryotic cells can either directly affect plasma membrane  
30 integrity or alternatively they may be internalized, translocated or injected inside the cells.  
31 Independent of their route, toxins induce modifications of cell morphology and/or provoke  
32 host-cell death. For example, the Anthrax Lethal Toxin (LT) is able to provoke pyroptosis or  
33 apoptosis, depending on the cell type and the LT concentration. Furthermore, at sub-lethal  
34 concentrations, it induces modification of the cytoskeleton and alters the distribution of  
35 junction proteins in endothelial and epithelial cells<sup>1</sup>. In Gram-negative bacteria, Type Three  
36 Secretion System (T3SS) toxins hijack eukaryotic signalling pathways, leading to damage  
37 ranging from modifications of the normal cytoskeleton function, to cell death, depending on  
38 the cell type and the toxin<sup>2</sup>.

39 Host-pathogen interaction studies therefore rely on detection and quantification of the  
40 bacteria-induced eukaryotic cell injuries. Plasma membrane permeabilization leading to cell  
41 death, the most dramatic outcome of the cell intoxication process, is usually monitored  
42 through the enzymatic measurement of lactate dehydrogenase released after plasma  
43 membrane rupture, or through the detection of nuclear stain incorporation by flow cytometry<sup>3-</sup>  
44 <sup>5</sup>. However, the analysis of early events such as the morphological changes induced by  
45 cytoskeleton rearrangements are usually based on fixed and stained cells, rendering fine  
46 kinetics studies laborious, or on expression of fluorescent chimeric markers, a time-  
47 consuming procedure to which some cells are refractory<sup>6</sup>. These approaches are not easily  
48 accessible to non-expert scientists.

49 Overall, there is a dearth of simple methods allowing real-time quantification of  
50 morphological changes or cell death. Here, we present the CLIQ-BID method, based on  
51 automated high-throughput monitoring of the fluorescence intensity of eukaryotic cell nuclei  
52 stained with vital-Hoechst. This live-imaging method permits real-time quantification of

53 bacteria-induced cell damage at single-cell resolution. Starting from an observation in the  
54 context of the *Pseudomonas aeruginosa* T3SS, it was extended to other Gram-positive and  
55 Gram-negative bacteria equipped with diverse virulence factors. Towards identification of  
56 new antibacterial therapeutic targets or research tools, this convenient approach could be  
57 employed in functional high-throughput screening of interference-RNA, bacterial strains,  
58 antibodies or small molecules. More generally, the CLIQ-BID method could also be used in  
59 other cytotoxicity and cell-stress studies.

60

## 61 RESULTS

### 62 ***P. aeruginosa* induces a quantifiable nuclei size reduction**

63 The injection of the exotoxins ExoS, T, Y and ExoU by the T3SS machinery is one of the  
64 main virulence determinants of *P. aeruginosa* clinical strains<sup>7</sup>. Those toxins have profound  
65 effects on eukaryotic cell biology, provoking plasma membrane disruption or inhibition of  
66 phagocytosis followed by a delayed apoptosis<sup>8</sup>. Visually, ExoS and ExoT action on host  
67 cytoskeleton leads to a reduction of cell area and a “shrinkage” phenotype<sup>9</sup>. In the search for  
68 robust descriptors of this phenomenon, we observed that the Hoechst-stained nuclei of Human  
69 Umbilical Vascular Endothelial Cells (HUVECs) become gradually smaller and brighter  
70 during incubation with the wild-type *P. aeruginosa* strain PAO1 harbouring ExoS and ExoT.  
71 In addition this increased intensity of nuclear staining remarkably correlated with the decrease  
72 of cell area (Fig. 1a, compare upper and lower images). The built-in Arrayscan image analysis  
73 workflow was employed in order to obtain the nuclei mask (Fig. 1a insert – magenta outlines)  
74 by intensity thresholding and the quantitative features corresponding to their areas and  
75 fluorescence intensities. The graphical representation of these features extracted from 70  
76 nuclei at different time points clearly shows a negative correlation between nuclei area and

77 intensity (Fig. 1b). Indeed, the condensation of the nuclei results in an increased concentration  
78 of the fluorescent dye complexed to the DNA and thus in an enhanced fluorescence intensity.  
79 Furthermore, a nuclear intensity threshold could readily be set to segregate cells with bright  
80 nuclei (Fig. 1c). Therefore, a subpopulation of cells displaying bright nuclei, which  
81 corresponds to the shrunk cells, could be automatically identified by monitoring the nuclear  
82 staining intensity.

83 In order to determine whether the observed nuclei condensation was a phenomenon restricted  
84 to HUVECs, the experiment was repeated on CHO, NIH 3T3, HeLa and A549 cells. Despite  
85 slight differences in kinetics between the cell types, the nuclear staining intensity increased  
86 during the time course of infection by *P. aeruginosa* (Supplementary Fig. S1 and  
87 Supplementary Video S1). Of importance, increased brightness was strictly correlated with  
88 cell shrinkage (compare upper and lower images of Supplementary Fig. S1).

89 *P. aeruginosa* induces a nuclear condensation that is responsible for the observed increase in  
90 nuclear staining intensity. A statistical analysis was performed in order to determine which of  
91 the nuclear features (i.e. area versus average intensity) better distinguishes between condensed  
92 and non-altered populations. To that end, images from uninfected and 3h-infected cells were  
93 obtained at 20x and 5x magnifications. Next, the nuclei images were analysed and three  
94 features were compared: the mean nuclear area, the mean nuclear intensity and the percentage  
95 of bright nuclei, which is the proportion of nuclei whose intensity is above a fixed threshold.  
96 These three parameters were the most promising among the different features calculated by  
97 the built-in software from the experiment described in Figure 1. The ability of these three  
98 parameters to discriminate between the images obtained at the beginning and at the end of the  
99 infection was assessed through the  $Z'$ -factor (abbreviated  $Z'$ ). This statistical coefficient takes  
100 into consideration the standard deviations as well as the difference between the means of the  
101 positive and negative controls, and is often used for the optimization and validation of High

102 Throughput Screening assays<sup>10</sup>. The values reported in Supplementary Table S1 clearly  
103 indicate that the percentage of bright nuclei is the most discriminant parameter with  $Z'=0.64$   
104 for 20x magnification, and that taking images at 5x magnification further increases the power  
105 of the test ( $Z'=0.75$ ).

106 The vital nuclear staining used here offers the possibility to monitor modifications of the  
107 nuclei by live-imaging during infection. To obtain live kinetics, the nuclei of the five cell  
108 types were labelled prior to infection with *P. aeruginosa* and images were taken at 5x  
109 magnification every 15 minutes for 4 hours. Images of the same fields at one hour interval are  
110 presented (Fig. 2a). Afterward, automated segmentation of the nuclei and measurement of  
111 fluorescence intensities were performed as described above and the percentages of bright  
112 nuclei were extracted from the built-in software. To visualize the cells that were considered to  
113 be damaged upon bacterial infection, nuclei with intensities above a fixed threshold were  
114 delineated in green while those below the threshold were delineated in magenta (Fig. 2a –  
115 inserts). Nuclei segmentation and thresholding based on vital-Hoechst staining intensity  
116 properly reflected the observed appearance of bright nuclei during the progression of  
117 infection. Furthermore, images show that nuclei condensation of 3T3, HeLa and A549 cells  
118 occurred earlier than for HUVEC and CHO cells. This was confirmed by the kinetic plots  
119 (Fig. 2b) that successfully detected an increase of bright nuclei, occurring exponentially with  
120 the duration of cell infection. These plots further depicted differences between cells in terms  
121 of inflection time and curve steepness. It was therefore possible to identify kinetics signatures  
122 for each of the five cell types. The method was named CLIQ-BID, standing for Cell Live  
123 Imaging Quantification of Bacteria Induced Damage.

124

125 **Detection of bright nuclei is highly discriminant**

126 We then focused our analysis on HUVECs which are particularly relevant because they are  
127 primary human cells, forming a polarized monolayer. The action of *P. aeruginosa* on  
128 HUVECs have been extensively studied by cellular biology and the morphological changes  
129 observed during infection have been described by microscopy approaches<sup>9,11-15</sup>. Furthermore,  
130 a “cell area” assay based on the quantification of fixed cells’ area by immunofluorescence  
131 staining was previously reported<sup>9,14</sup>. Therefore, we investigated how the CLIQ-BID method  
132 compares to the previously published method which is based on immunofluorescence cell  
133 staining. For this purpose, HUVECs were infected for different time periods, their nuclei were  
134 observed with vital Hoechst staining and then immediately fixed, immunostained and  
135 observed at the same position in the wells. A comparison of the results obtained with the  
136 CLIQ-BID and “cell area” quantification methods is presented in Figure 3. Nuclei were  
137 segmented and discriminated based on their fluorescence intensities (Fig. 3a, Hoechst and  
138 bright nuclei images) while the cells’ area was quantified based on thresholding of the  
139 vinculin staining (Fig. 3a, Vinculin and cell area images). Indeed, the area covered by the  
140 cells decreased during infection with *P. aeruginosa*, in agreement with previous  
141 observations<sup>14</sup>. Furthermore, the plots of the percentage of bright nuclei and the percentage of  
142 the field area cleared by the cells after different infection durations exhibit a similar trend and  
143 the correlation coefficient between the readouts of the image pairs was 0.96. However, the  
144 standard deviations were much lower for the percentage of bright nuclei than for the cell area  
145 (Figure 3b).

146 In order to confirm that the CLIQ-BID method reduces the variation between individual data  
147 points, the comparison experiment was repeated with two modifications: i) the number of  
148 replicate wells was set to 30 per condition and ii) the HUVECs were infected for 3 hours  
149 either with a wild-type *P. aeruginosa* strain or the  $\Delta pscF$  strain, which is unable to produce  
150 the T3SS toxin injection needle and is therefore deficient for a functional T3SS. This

151 experiment substantiated that the CLIQ-BID method produces more robust and discriminant  
152 results with a  $Z'$ -factor equal to 0.89 versus 0.14 for the cell area method (Supplementary  
153 Table S2).

154 The high  $Z'$ -factor obtained with the CLIQ-BID method indicated that it is well-suited for  
155 high throughput screening. To further examine this possibility, cell infections with wild-type  
156 or  $\Delta pscF$  *P. aeruginosa* strains were compared in 96- and 384-well plates. The live-imaging  
157 monitoring of nuclei intensities allowed the obtaining of reproducible kinetics curves in the 48  
158 replicates (Supplementary Fig. S2). Indeed, the  $Z'$ -factor values obtained by comparing the  
159 wild-type and the T3SS deficient strains were close to or above 0.9 for both plate formats.

160 Importantly, an additional 384-well plate was inoculated with overnight *P. aeruginosa*  
161 cultures, as opposed to exponential phase cultures, which is currently used to detect T3SS  
162 activity (Supplementary Fig. S2). The removal of the subculture step significantly reduces the  
163 handling procedure in the perspective of bacteria or molecule library screens. Despite higher  
164 variation than with exponential cultures, the  $Z'$ -factor displayed values close to 0.8, higher  
165 than the gold-standard of 0.7 above which a library could be screened in a single replicate  
166 with an acceptable risk of false-positives and -negatives. Taken together, these results indicate  
167 that the newly-developed CLIQ-BID method is adapted for HTS strategies.

168 In the search for a global descriptor of each kinetics plot, the Area Under the Curve (AUC)  
169 was selected. As expected, large differences were observed between AUC obtained from  
170 wells infected with wild-type or T3SS deficient strains (Supplementary Fig. S3). Indeed, the  
171 statistical analysis showed that the AUC can robustly discriminate between infections by  
172 these two strains, with  $Z'$ -factor values of 0.77 and 0.63 in 96- and 384-well plates,  
173 respectively (Supplementary Table S3).

174

175 **Bright nuclei detection enables potent screening strategies**

176 Considering the encouraging results, the potential of the method to screen for inhibitors of  
177 bacteria-induced cell damage was further investigated on a panel of molecules. In this proof-  
178 of-concept experiment, compounds targeting the bacteria or the eukaryotic cells were tested,  
179 along with siRNA. A major improvement was also made with the use of bacteria  
180 constitutively expressing GFP in their cytosol. Measuring the global GFP fluorescence  
181 increase in the wells thus enables the detection of possible bacteriostatic/bactericidal  
182 properties of the tested compounds. These experiments were therefore analysed by plotting  
183 the kinetics curves of bright nuclei (cell toxicity) and GFP fluorescence (bacterial growth), as  
184 represented in Figure 4.

185 Cell damage were significantly delayed by known inhibitors of *P. aeruginosa* T3SS, like the  
186 small molecule MBX2401 or polyclonal antibodies raised against the tip protein PcrV<sup>16,17</sup>.  
187 Conversely, neither DMSO nor antibodies targeting the translocator PopB had any effect on  
188 the cell infection, as expected (Fig. 4a). Among molecules targeting the eukaryotic cells, the  
189 prostaglandin PGE2 and forskolin, a cAMP inducer recently shown to inhibit *P. aeruginosa*  
190 T3SS effects through Rap1 activation<sup>12</sup>, significantly delayed the kinetics (Fig. 4c). On the  
191 other hand staurosporine and chelerythrine, two potent cytotoxic inhibitors of protein  
192 kinases<sup>18,19</sup>, immediately induced the appearance of bright nuclei. Other compounds  
193 moderately accelerated cell damage during infection, namely H-89 (protein kinase A  
194 inhibitor), sphingosine-1-P (signalling phospholipid) and NSC23766 (Rac1 inhibitor), while  
195 wortmannin (PI3-K inhibitor) had no effect. Of note, cells incubated with H-89, sphingosine-  
196 1-P and Forskolin in the absence of bacteria exhibited a higher basal level of bright nuclei  
197 (Supplementary Fig. S4). This moderate toxicity could explain the accelerated kinetics  
198 observed when cell were infected in the presence of H-89 and sphingosine-1-P and the  
199 relatively high baseline observed with forskolin at the beginning of cell infection. Finally, cells

200 were grown after transfection with arbitrarily chosen siRNAs from a laboratory collection and  
201 were subsequently infected. From the 18 tested siRNAs, some had no effect while some  
202 exhibited promoting or inhibiting activities (Fig. 4e). The validation and the biological  
203 investigation of the role of their targets are beyond the scope of this work.

204 Observing the effect of a particular treatment on bacteria growth (Fig. 4b, d, f) allowed the  
205 determination as to whether any virulence inhibition was related to an antibiotic effect.  
206 Indeed, none of the eukaryotic nor T3SS-specific targeting compounds exhibited a  
207 bacteriostatic effect, while the antibiotic gentamicin prevented bacterial growth and,  
208 consequently, host cell intoxication. Furthermore, the synthetic descriptors of the cell toxicity  
209 and bacterial kinetics curves (respective AUCs) permitted the straightforward statistical  
210 comparison of the kinetics by one-way ANOVA (Supplementary Fig. S5). In conclusion, the  
211 developed method enables the identification of promotional or inhibitory effects from a  
212 variety of molecular categories (small organic molecules, antibodies and siRNAs) and allows  
213 one to simultaneously counter-screen for antibiotic effects.

214 Finally, the method was employed to compare the effects of different bacterial strains and  
215 bacterial species. For this purpose, HUVECs were infected with 16 different bacteria and the  
216 intensities of cell nuclei were monitored by live-imaging. Kinetics plots and the  
217 corresponding AUCs (Fig. 5) show the diverse virulence potential of these bacteria. Among  
218 the *P. aeruginosa* strains, the PP34 strain, injecting through its T3SS the powerful  
219 phospholipase toxin ExoU<sup>3,7,20</sup>, was the most active followed by IHMA87 and  
220 PAO1 $\Delta$ *pscD::exlBA* (PAO1 *exlBA*) strains expressing the recently discovered Two Partner  
221 Secreted toxin ExlA<sup>21-23</sup> and the CHA reference strain used throughout this study. Of interest,  
222 the *Serratia marcescens* strain expressing the ShlA toxin<sup>24</sup> homolog to ExlA was as active as  
223 the PP34 strain, while the isogenic mutant strain that has a transposon inserted into the *shlB*  
224 gene<sup>25</sup>, did not induce the appearance of bright nuclei. In *Staphylococcus aureus*, the 8325-4

225 strain exhibited lower effects than the closely related USA300 BEZIER and SF8300 strains,  
226 both from the USA300 lineage known to be highly virulent<sup>26</sup>. This workflow was also  
227 successful in detecting cellular damage caused by *Yersinia enterocolitica*, which correlated  
228 with its T3SS since the mutant depleted of T3SS toxins exhibited a significantly lower  
229 activity. Finally, five bacteria species did not display measurable effects toward the  
230 eukaryotic cells under the used experimental conditions, notably the relatively short time span  
231 of infection and low MOI. Of interest, the statistical analysis of AUCs derived from the  
232 kinetics plots of each replicate confirmed the depicted intra-species differences (Fig. 5b). The  
233 sigmoid curves obtained with the virulent bacteria display different shapes, notably regarding  
234 the lag phase and the slope. These parameters are not expected to be correlated because  
235 different virulence mechanisms triggers effects with different delays and different degrees of  
236 synchronicity in the target cell population. The AUCs calculation does not give access to  
237 these variations and it is conceivable that they could compensate, resulting in some cases in  
238 similar AUCs for different curve shapes. Therefore, the curves of each replicate of the same  
239 experiment were fitted using a sigmoid equation and the calculated inflection points and curve  
240 steepness were represented on a XY plot for each bacteria species (Fig. 5c). This analysis  
241 clearly highlights inter- and intra-species differences while similar strains within *P.*  
242 *aeruginosa* (PAO1 *exlBA* and IHMA87) and *S. aureus* (SF8300 and USA300) species  
243 clustered together. Overall, real-time imaging allowed the observation of different cell-  
244 damage kinetics, which are in agreement with what is expected for the corresponding bacteria  
245 featuring diverse toxins and virulence mechanisms.

246

## 247 DISCUSSION

248 The new high-throughput image analysis strategy described in this work exhibits great  
249 potential for monitoring cell damage induced by bacteria, as well as by other mechanisms.

250 Through nuclei monitoring, the method allows the observation of cell-reaction to Gram-  
251 positive and Gram-negative bacteria secreting or injecting toxins. Furthermore, both cell lysis  
252 induced by plasma-membrane targeting toxins ExoU and ExlA<sup>20,22</sup>, as well as cell shrinkage  
253 induced by ExoS<sup>9,27</sup> were readily detected. Of note, this method can also be employed to  
254 reveal cytotoxicity or cell stress from a variety of origins, as exemplified by the detection of  
255 the effects of chelerythrine and staurosporine known to promote apoptosis. It is thus able to  
256 detect cell shrinkage, necrosis and apoptosis.

257 The developed method allows cost-effective kinetic measurements of bacteria-induced action  
258 on several cell lines, requiring a simple staining procedure, a microscope and an image-  
259 analysis software. Detection of nuclei and quantification relies on the widely-used Hoechst  
260 33342, an inexpensive vital stain of cell nuclei used for almost four decades<sup>28</sup>. After image  
261 acquisition on the microscope, images may be analysed with standard software like Cell  
262 Profiler, ImageJ or Fiji<sup>29-31</sup>, using basic algorithms to delineate nuclei and measure their  
263 fluorescence intensities. In our work, we used an automated microscope along with its  
264 proprietary analysis software to demonstrate the great potential of this method for High  
265 Content Screening.

266 Indeed the  $Z'$ -factor values obtained in different assay configurations were often above 0.8.  
267 This statistical descriptor reflects the quality of a screening method, i.e. its ability to identify  
268 “hits”<sup>10</sup>. Screening of libraries are undertaken only if the  $Z'$ -factor is above 0.6 and a value  
269 above 0.7 is considered to be fully satisfactory. The elevated  $Z'$ -factor value obtained in 384-  
270 well microplates with fresh or overnight cultures of bacteria indicated that this assay could be  
271 employed to screen large bacterial mutant or eukaryotic CRISPR/Cas9 libraries. Furthermore,  
272 the screening approach was successfully applied to a set of antibodies and small molecules  
273 targeting either bacteria or eukaryotic cells and to a panel of siRNAs. Indeed, it identified  
274 three inhibitory activities among the tested small molecules and antibodies: the MBX2401

275 drug and anti-PcrV antibodies, both known to inhibit *P. aeruginosa* T3SS<sup>16,17</sup>, and forskolin,  
276 known to counteract the T3SS effect in eukaryotic cells<sup>12</sup>. This represents a proof of concept  
277 for a screening strategy. Moreover, the morphological readout of the method (brightness of  
278 the nuclei) is a downstream event in the infection process, enabling the screening of  
279 molecules that could target early or late events in the bacteria or the host.

280 In addition, the simultaneous quantification of GFP-expressing bacteria allows one to counter-  
281 screen, in the same test, for bacteriostatic/bactericidal activities. Moreover, the same CLIQ-  
282 BID method can be used in the absence of bacteria to detect the potential deleterious effects  
283 of screened compounds. Therefore, this method can be the basis of a powerful 3-in-1  
284 approach to rapidly identify treatments inhibiting bacteria virulence without affecting their  
285 growth capacities or the eukaryotic cells' integrity. This is of particular interest since the  
286 search for antivirulence treatments is receiving growing attention because they are thought to  
287 reduce the risk of resistance emergence and microbiome destabilization<sup>32,33</sup>.

288 The increasing accessibility to HCS/HCA equipment, with the help of the simple and cost-  
289 effective CLIQ-BID method described here, should foster the understanding of bacterial  
290 virulence as well as other scientific areas where early cell damage and cell stress are of  
291 interest.

## 292 METHODS

### 293 **Bacteria strains**

294 *Pseudomonas aeruginosa* strains CHA, PAO1 $\Delta$ *pscD::exlBA*, IHMA87 and PP34; and  
295 *Serratia marcescens* Db11 and Db11-tn-*shlB* were from our lab collection and previously  
296 published<sup>14,21,22,25</sup>. *Staphylococcus aureus* strains SF8300, USA300 BEZIER and 8325-4 were  
297 a kind gift from Dr Karen Moreau. Other strains were *Yersinia enterocolitica* E40 and  
298  $\Delta$ HOPEMN<sup>17</sup>, *Acinetobacter sp. genomospecies 13* ATCC 23220, *Burkholderia cepacia*

299 ATCC 17616, *Pseudomonas putida* KT2442, *Pseudomonas fluorescens* BG1 (environmental  
300 isolate, gift from Dr John Willison) and *Stenotrophomonas maltophilia* (ATCC 13637).  
301 Bacteria were grown in LB (Luria Bertani - Difco) except for *S. aureus* which were grown in  
302 BHI (Brain Heart Infusion – Difco). *Y. enterocolitica* strains were grown at 28 °C and the  
303 other strains at 37 °C. Unless otherwise stated, cultures were grown overnight under shaking  
304 at 300 rpm and then diluted in fresh media to an optical density measured at 600 nm (OD<sub>600</sub>)  
305 of 0.1. When cultures reached OD<sub>600</sub> of 1, typically after 2.5 h of growth under shaking,  
306 bacteria were mixed with eukaryotic cells at a multiplicity of infection (MOI) of 10.

### 307 **Chemicals and antibodies**

308 Hoechst 33342, Gentamicin, H-89, Sphingosine-1-P, Prostaglandin E2, Staurosporine,  
309 Forskolin, NSC23766 and Wortmannin were from Sigma-Aldrich and chelerythrine from  
310 Merck Millipore. MBX2401, an inhibitor of the Type Three Secretion System (T3SS) from *P.*  
311 *aeruginosa*<sup>16</sup> was synthesized as previously described<sup>34</sup>. Antibodies raised against *P.*  
312 *aeruginosa* PopB and PcrV (anti-PopB and anti-PcrV) were obtained in our laboratory and  
313 previously characterized<sup>17</sup>. Antibodies to Vinculin were from Santa Cruz and the secondary  
314 antibodies coupled to Alexa 488 were purchased from Molecular Probes.

### 315 **Cell culture**

316 Human umbilical vein endothelial cells (HUVECs) were isolated according to previously  
317 described protocols<sup>9</sup>. The use of umbilical cords for scientific purposes is authorized by the  
318 L1211-2 act from the French Public Health Code. Written informed consent was obtained  
319 from each woman who donated an umbilical cord. The privacy of the donor's personal health  
320 information was protected. Recovered cells were cultured in endothelial-basal medium 2  
321 (EBM-2; Lonza) supplemented as recommended by the manufacturer. A549 (CCL-185) and  
322 HeLa (CCL-2) cells were grown in RPMI supplemented with 10% foetal calf serum. 3T3

323 (CRL-2752) and CHO K1 (CCL-61) cells were grown in DMEM and F12 medium,  
324 respectively, supplemented with foetal calf serum.

### 325 **siRNA**

326 Cells were seeded at 12,500 cells per/well in a 96-well plate and transfected with siRNAs  
327 using Lipofectamine™ RNAiMax transfection reagent (Thermo Fisher Scientific), according  
328 to the Reverse Transfection manufacturer's protocol. Briefly, 2.5 pmol of siRNA were diluted  
329 in 10 µl of supplemented EBM-2 and mixed with 0.2 µl of transfection reagent, pre-diluted in  
330 9.8 µl of supplemented EBM-2. After 15min at room temperature, the complexes were added  
331 to the cells in a final volume of 100 µl of supplemented EBM-2. Cells were used 48 h later.

### 332 **Cell treatments, Hoechst staining and infection**

333 Black µclear 96-well plates (Greiner) were seeded at 12,500 cells per/well. Black µclear 384-  
334 well plates (Greiner) were seeded at 3,000 cells per well. Cells were used 48 h later to obtain  
335 highly confluent monolayers. Medium was replaced 3 h before infection with fresh medium  
336 containing Hoechst 33342 (1 µg/ml). After incubation during 1 h, two washes with 80 µl of  
337 fresh non-supplemented EBM-2 medium. All media were pre-heated at 37 °C.

338 For pharmacological and antibody treatments, medium was replaced 30 min before infection  
339 with 80 µl of fresh medium supplemented with: gentamicin 200 µg/ml, H-89 10 µM,  
340 sphingosine-1-P 2 µg/ml, prostaglandin E2 1 nM, staurosporine 1 µM, forskolin 10 µM,  
341 NSC23766 50 µM, wortmannin 1 µM, chelerythrine 1 µM, MBX2401 and MBX2402 30 µM.  
342 When applicable, the final DMSO concentration was 0.5%. Sera containing antibodies  
343 directed against PopB and PcrV were diluted to a final concentration of 5%.

344 Cells were infected at a multiplicity of infection (MOI) of 10 by adding 20 µl of EBM-2  
345 containing a 5x concentrated bacteria suspension. Plates were immediately observed by  
346 Arrayscan microscopy.

## 347 **Automated High Content Imaging and High Content Analysis (HCA)**

348 The image acquisitions were performed on an automated microscope ArrayScanVTI (Thermo  
349 Scientific) using a Zeiss 20x (NA 0.4) LD Plan-Neofluor or a Zeiss 5x (NA 0.25) Fluar air  
350 objectives. In 96-well plates, four images per well were acquired with the 20x or 5x objectives  
351 and one image per well was acquired with the 5x objective in 384-well plates. The dichroic  
352 mirror used for Hoechst staining was BGRFR-386/23 nm and BGRFR-brightfield for  
353 transmitted light imaging. Exposure times were set to reach 40% of intensity saturation in the  
354 reference wells at the beginning of the experiment. The microplate was maintained at 37°C  
355 and 5% CO<sub>2</sub> in the ArrayScan Live Cell Module and images were automatically acquired  
356 every 15 min for up to five hours. Indicated times refer to the actual time of image acquisition  
357 and are adjusted for delay between wells due to the plate displacement. Typically five minutes  
358 are required to scan a complete 96-well plate.

359 Quantification of nuclei parameters was made using the Cell Health Profiling Bio-Application  
360 of Thermo Scientific HCS Studio v6.5.0. Each nucleus was detected in the Hoechst channel  
361 with the isodata thresholding method. Border-touch nuclei were rejected from each image.  
362 Nuclei area and nuclei average intensity features, respectively named ObjectAreaCh1 and  
363 ObjectAvgIntenCh1, were automatically calculated. When indicated in the text, a threshold  
364 was applied on the ObjectAvgIntenCh1 feature to discriminate the population of cells with  
365 bright nuclei. This threshold was set to 2,100 or 1,200 fluorescence arbitrary units (a.u.) for  
366 20x or 5x magnification images respectively, and the proportion of cells with bright nuclei  
367 were automatically calculated and named %HIGH\_ObjectAvgIntenCh1. The arbitrary units  
368 correspond to the raw fluorescence intensities obtained through the HCS Studio software.

## 369 **Immunofluorescence staining and quantification**

370 Cells were washed, fixed with 4% paraformaldehyde for 15 min, permeabilized with 0.5%  
371 Triton X-100 for 5 min and labelled with a mouse anti-Vinculin 7F9 primary antibody (Santa  
372 Cruz) and donkey anti-mouse Cy3 secondary antibody (Jackson ImmunoResearch  
373 Laboratories) for 1 h each. Nuclei were labelled with Hoechst 33258 (10 µg/ml, Sigma-  
374 Aldrich). Under these conditions, total cellular vinculin is detected yielding a whole-cell  
375 labelling. Images were captured using an automated microscope ArrayScanVTI with the 5x  
376 magnification objective, in the BGRFR-549/15 nm channel, and treated with ImageJ software.  
377 Briefly, images of vinculin staining were binarized and the total cell area was calculated for  
378 each image. To facilitate interpretation, results were shown as the percentage of the field area  
379 cleared by the cells.

## 380 **Statistics**

381 To evaluate the quality of the assay and its ability to identify “hits”, the  $Z'$ -factor was  
382 calculated using the following equation, as described by Zhang et al <sup>10</sup>:

$$383 \quad (1) Z' = 1 - 3 * (\sigma_p + \sigma_n) / |\mu_p - \mu_n|$$

384 where  $\sigma_p$  and  $\sigma_n$  are the standard deviations of the positive and negative conditions,  
385 respectively, and  $\mu_p$  and  $\mu_n$  are the means of the positive and negative conditions,  
386 respectively.

387 Statistical analyses were performed using SigmaPlot 12.5 (Systat software) for the  
388 comparison of multiple groups by one-way ANOVA (two-tailed). When appropriate, *post hoc*  
389 tests were Tukey or Dunnett for multiple comparisons or comparison to the control group,  
390 respectively.

391 In figure legends, n represents the number of well replicates.

392 Curve fitting was done with SigmaPlot 12.5 using the following equation:

393 
$$(2) y = y_0 + \frac{a}{1 + e^{-b(x-x_0)}}$$

394 where  $y_0$  and  $a$  are the minimal and the range values of the bright nuclei percentage,  
395 respectively, and  $x_0$  and  $b$  respectively correspond to the inflection time and the curve  
396 steepness.

397 **Data availability**

398 The datasets generated during and/or analysed during the current study are available from the  
399 corresponding author on reasonable request.

400 REFERENCES

- 401 1. Moayeri, M. & Leppla, S. H. Cellular and systemic effects of anthrax lethal toxin and  
402 edema toxin. *Mol. Aspects Med.* **30**, 439–455 (2009).
- 403 2. Dean, P. Functional domains and motifs of bacterial type III effector proteins and their  
404 roles in infection. *FEMS Microbiol. Rev.* **35**, 1100–1125 (2011).
- 405 3. Bucior, I., Tran, C. & Engel, J. Assessing *Pseudomonas* Virulence Using Host Cells. in  
406 *Pseudomonas Methods and Protocols* (eds. Filloux, A. & Ramos, J.-L.) **1149**, 741–755  
407 (Springer New York, 2014).
- 408 4. Chan, F. K.-M., Moriwaki, K. & De Rosa, M. J. Detection of necrosis by release of  
409 lactate dehydrogenase activity. *Methods Mol. Biol. Clifton NJ* **979**, 65–70 (2013).
- 410 5. Jiang, L. *et al.* Monitoring the progression of cell death and the disassembly of dying cells  
411 by flow cytometry. *Nat. Protoc.* **11**, 655–663 (2016).
- 412 6. Riedl, J. *et al.* Lifeact: a versatile marker to visualize F-actin. *Nat. Methods* **5**, 605–607  
413 (2008).
- 414 7. Berthelot, P. *et al.* Genotypic and phenotypic analysis of type III secretion system in a  
415 cohort of *Pseudomonas aeruginosa* bacteremia isolates: evidence for a possible  
416 association between O serotypes and exo genes. *J. Infect. Dis.* **188**, 512–518 (2003).
- 417 8. Hauser, A. R. The type III secretion system of *Pseudomonas aeruginosa*: infection by  
418 injection. *Nat. Rev. Microbiol.* **7**, 654–665 (2009).
- 419 9. Huber, P., Bouilliot, S., Elsen, S. & Attrée, I. Sequential inactivation of Rho GTPases and  
420 Lim kinase by *Pseudomonas aeruginosa* toxins ExoS and ExoT leads to endothelial  
421 monolayer breakdown. *Cell. Mol. Life Sci. CMLS* **71**, 1927–1941 (2014).
- 422 10. Zhang, J.-H., Chung, T. D. Y. & Oldenburg, K. R. A Simple Statistical Parameter for Use  
423 in Evaluation and Validation of High Throughput Screening Assays. *J. Biomol. Screen.* **4**,  
424 67–73 (1999).

- 425 11. Assis, M.-C. *et al.* Up-regulation of Fas expression by *Pseudomonas aeruginosa*-infected  
426 endothelial cells depends on modulation of iNOS and enhanced production of NO  
427 induced by bacterial type III secreted proteins. *Int. J. Mol. Med.* **18**, 355–363 (2006).
- 428 12. Bouillot, S., Attrée, I. & Huber, P. Pharmacological activation of Rap1 antagonizes the  
429 endothelial barrier disruption induced by exotoxins ExoS and ExoT of *Pseudomonas*  
430 *aeruginosa*. *Infect. Immun.* **83**, 1820–1829 (2015).
- 431 13. De Assis, M.-C., Saliba, A. M., Vidipó, L. A., De Salles, J. B. & Plotkowski, M.-C.  
432 *Pseudomonas aeruginosa*-induced production of free radicals by IFN $\gamma$  plus  
433 TNF $\alpha$ -activated human endothelial cells: mechanism of host defense or of bacterial  
434 pathogenesis? *Immunol. Cell Biol.* **82**, 383–392 (2004).
- 435 14. Golovkine, G. *et al.* VE-cadherin cleavage by LasB protease from *Pseudomonas*  
436 *aeruginosa* facilitates type III secretion system toxicity in endothelial cells. *PLoS Pathog.*  
437 **10**, e1003939 (2014).
- 438 15. Saliba, A. M. *et al.* Type III secretion-mediated killing of endothelial cells by  
439 *Pseudomonas aeruginosa*. *Microb. Pathog.* **33**, 153–166 (2002).
- 440 16. Bowlin, N. O. *et al.* Mutations in the *Pseudomonas aeruginosa* needle protein gene pscF  
441 confer resistance to phenoxyacetamide inhibitors of the type III secretion system.  
442 *Antimicrob. Agents Chemother.* **58**, 2211–2220 (2014).
- 443 17. Goure, J., Broz, P., Attree, O., Cornelis, G. R. & Attree, I. Protective anti-V antibodies  
444 inhibit *Pseudomonas* and *Yersinia* translocon assembly within host membranes. *J. Infect.*  
445 *Dis.* **192**, 218–225 (2005).
- 446 18. Herbert, J. M., Augereau, J. M., Gleye, J. & Maffrand, J. P. Chelerythrine is a potent and  
447 specific inhibitor of protein kinase C. *Biochem. Biophys. Res. Commun.* **172**, 993–999  
448 (1990).

- 449 19. Tamaoki, T. *et al.* Staurosporine, a potent inhibitor of phospholipid/Ca<sup>++</sup>-dependent  
450 protein kinase. *Biochem. Biophys. Res. Commun.* **135**, 397–402 (1986).
- 451 20. Sato, H. & Frank, D. W. ExoU is a potent intracellular phospholipase: ExoU  
452 phospholipase activity. *Mol. Microbiol.* **53**, 1279–1290 (2004).
- 453 21. Basso, P. *et al.* *Pseudomonas aeruginosa* Pore-Forming Exolysin and Type IV Pili  
454 Cooperate To Induce Host Cell Lysis. *mBio* **8**, (2017).
- 455 22. Elsen, S. *et al.* A type III secretion negative clinical strain of *Pseudomonas aeruginosa*  
456 employs a two-partner secreted exolysin to induce hemorrhagic pneumonia. *Cell Host*  
457 *Microbe* **15**, 164–176 (2014).
- 458 23. Reboud, E. *et al.* Phenotype and toxicity of the recently discovered exlA-positive  
459 *Pseudomonas aeruginosa* strains collected worldwide. *Environ. Microbiol.* (2016).  
460 doi:10.1111/1462-2920.13262
- 461 24. Poole, K., Schiebel, E. & Braun, V. Molecular characterization of the hemolysin  
462 determinant of *Serratia marcescens*. *J. Bacteriol.* **170**, 3177–3188 (1988).
- 463 25. Kurz, C. L. *et al.* Virulence factors of the human opportunistic pathogen *Serratia*  
464 *marcescens* identified by in vivo screening. *EMBO J.* **22**, 1451–1460 (2003).
- 465 26. Diep, B. A. *et al.* Contribution of Panton-Valentine Leukocidin in Community-Associated  
466 Methicillin-Resistant *Staphylococcus aureus* Pathogenesis. *PLoS ONE* **3**, e3198 (2008).
- 467 27. Sun, J. & Barbieri, J. T. ExoS Rho GTPase-activating protein activity stimulates  
468 reorganization of the actin cytoskeleton through Rho GTPase guanine nucleotide  
469 disassociation inhibitor. *J. Biol. Chem.* **279**, 42936–42944 (2004).
- 470 28. Arndt-Jovin, D. J. & Jovin, T. M. Analysis and sorting of living cells according to  
471 deoxyribonucleic acid content. *J. Histochem. Cytochem. Off. J. Histochem. Soc.* **25**, 585–  
472 589 (1977).

- 473 29. Schindelin, J. *et al.* Fiji: an open-source platform for biological-image analysis. *Nat.*  
474 *Methods* **9**, 676–682 (2012).
- 475 30. Schneider, C. A., Rasband, W. S. & Eliceiri, K. W. NIH Image to ImageJ: 25 years of  
476 image analysis. *Nat. Methods* **9**, 671–675 (2012).
- 477 31. Kamentsky, L. *et al.* Improved structure, function and compatibility for CellProfiler:  
478 modular high-throughput image analysis software. *Bioinformatics* **27**, 1179–1180 (2011).
- 479 32. Clatworthy, A. E., Pierson, E. & Hung, D. T. Targeting virulence: a new paradigm for  
480 antimicrobial therapy. *Nat. Chem. Biol.* **3**, 541–548 (2007).
- 481 33. Johnson, B. K. & Abramovitch, R. B. Small Molecules That Sabotage Bacterial  
482 Virulence. *Trends Pharmacol. Sci.* (2017). doi:10.1016/j.tips.2017.01.004
- 483 34. Moir, D., Aiello, D., Peet, N., Williams, J. & Torhan, M. Inhibitors of Bacterial Type III  
484 Secretion System. (2013).
- 485

486 ACKNOWLEDGMENTS

487 Y.W. was a recipient of a postdoctoral fellowship from the Fondation pour la Recherche  
488 Médicale. This project was in part supported by grants from the AVIESAN T3SS (ANR  
489 PRP1.4), the Laboratory of Excellence GRAL (ANR-10-LABX-49-01) and the Agence  
490 Nationale de Recherche (ANR-15-CE11-0018-01). We acknowledge the Labex GRAL and  
491 IBiSA for financial support to the CMBA platform. Authors are grateful to Charles Ross  
492 Dunlop for proofreading the manuscript.

493

494 AUTHORS CONTRIBUTIONS

495 Y.W. and E.F. designed experiments, Y.W., S.B., P.H. and E.F. performed experiments, I.A.  
496 and E.S. contributed reagents and methods, Y.W., E.S., P.H., I.A. and E.F. analyzed and  
497 discussed the data and E.F. wrote the manuscript. All authors contributed to and edited the  
498 manuscript.

499

500 ADDITIONAL INFORMATION

501 Competing Interests: The authors declare that they have no competing interests.

502

503 FIGURE LEGENDS

504 **Figure 1: Smaller and brighter cell nuclei reflect *P. aeruginosa* induced cell-damage.**

505 Human primary endothelial cells (HUVECs) were infected with *P. aeruginosa* and monitored  
506 at different stages of infection by live-imaging microscopy with vital-Hoechst nuclear stain. a)  
507 Cell surface and cell nuclei observed in transmitted light and by fluorescent labelling, upper  
508 and lower images respectively, in the same field at one hour intervals. Nuclei from the same  
509 set of images were automatically segmented (insert – magenta outlines). The scale bars shown  
510 on the last nuclei image correspond to 50  $\mu\text{m}$ . b) The area and fluorescence intensities of each  
511 segmented nucleus were plotted. Data obtained from different time points are represented in  
512 colors, from green (0 min) to dark red (240 min). a.u. = arbitrary units. c) Nuclear staining  
513 intensities of cells at different time points of infection are represented in box plots. Whiskers  
514 indicate the 10th and 90th percentiles; the top and bottom lines represent the 25th and 75th  
515 percentiles; the middle line and dots respectively show median and outliers. Intensities from  
516 the three first time points are statistically different from those of the two last time points (one  
517 way ANOVA,  $P < 0.05$ ). The horizontal dashed line represent a threshold that could  
518 discriminate between normal and bright nuclei. In b) and c),  $n = 70$  cells at each time point.

519

520 **Figure 2: Live-imaging quantification of *P. aeruginosa* cell infection by fluorescence**

521 **intensity measurement of Hoechst-labelled nuclei.** HUVEC, CHO, 3T3, HeLa and A549

522 cells were labelled with vital-Hoechst prior to infection with *P. aeruginosa* and monitored by  
523 microscopy at a 5x magnification. a) Cell nuclei observed by fluorescent labelling and  
524 automatically segmented (insert). Nuclei with intensities below a fixed threshold were  
525 delineated in magenta while those above the threshold were delineated in green. The scale bar  
526 shown on the first image of the HUVECs cells corresponds to 200  $\mu\text{m}$ . b) Kinetic plots

527 representing the percentage of nuclei with intensities above the thresholds in the images taken  
528 every 15 min.

529

530 **Figure 3: Comparison of the CLIQ-BID and “cell area” methods.** HUVECs were infected  
531 with *P. aeruginosa* for different durations; images of the nuclei were acquired before cell  
532 fixation, immunostaining and acquisition of cell area images. a) Image sets at different time  
533 points for i) Hoechst: cell nuclei; ii) Bright nuclei: nuclei automatically segmented and sorted  
534 for intensities below (red) or above (green) a fixed threshold; iii) Vinculin: cell area detected  
535 with a cytoplasmic vinculin staining; iv) Cell area: automated thresholding of the  
536 immunostaining allowing the calculation of the field area covered by the cells. The scale bar  
537 shown on the last nuclei image corresponds to 50  $\mu\text{m}$ . b) Plots of the percentage of nuclei  
538 with intensities above the thresholds and of the percentage of area cleared by the cells after  
539 different infection durations. Error bars represent the standard deviation (n=8).

540

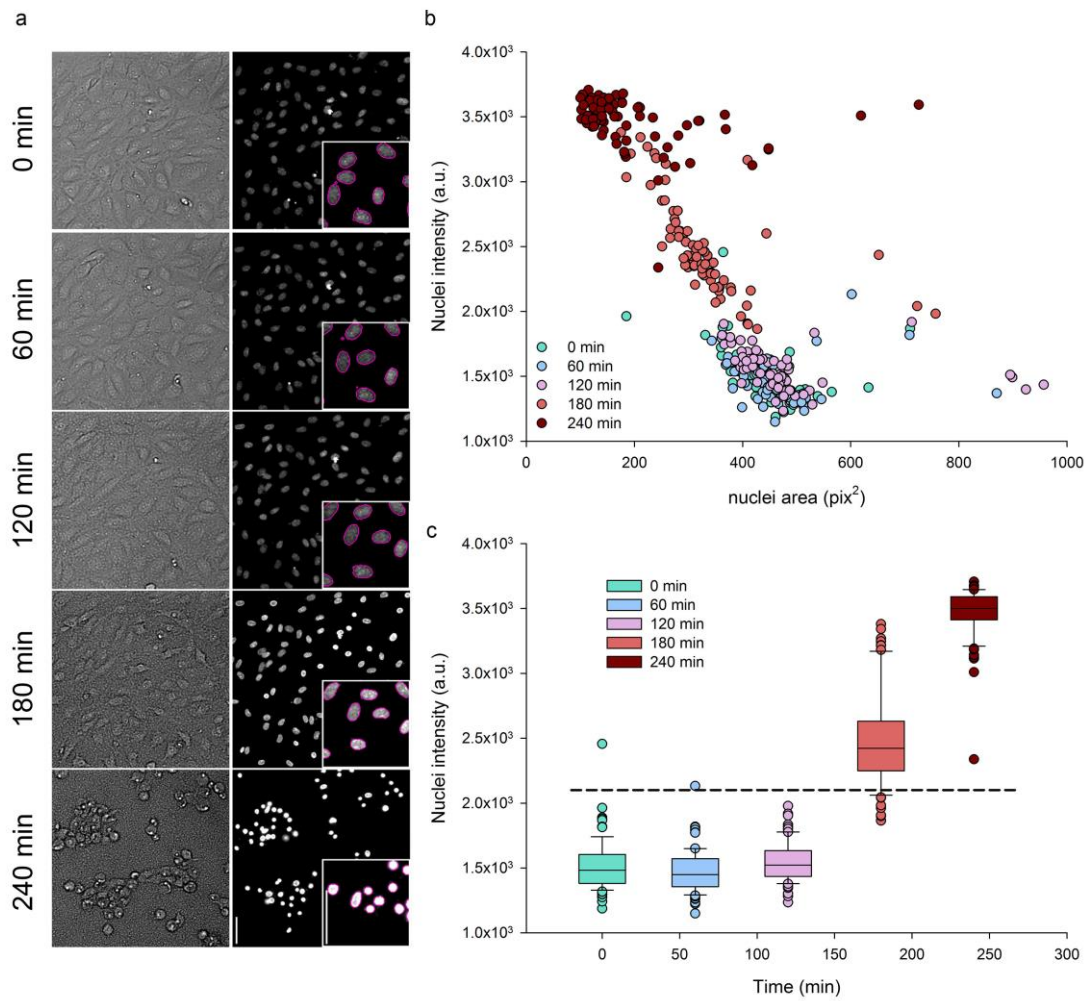
541 **Figure 4: Screening of a panel of molecules.** HUVECs were infected with *P. aeruginosa*  
542 wild-type strain in the presence of molecules targeting the bacteria (a, b) or targeting the  
543 eukaryotic cells (c, d) and their respective controls. To assess the effect of siRNA transfection  
544 in the cells, HUVECs were transfected two days before infection (e, f). A strain deficient for  
545 the production of the T3SS needle subunit ( $\Delta pscF$ ) was used as control. The kinetics of bright  
546 nuclei appearance (a, c, e) and bacteria growth (b, d, f) were simultaneously recorded by live-  
547 imaging and analysed. a.u. = arbitrary units.

548

549 **Figure 5: Comparison of cell damage kinetics with different bacteria.** HUVECs were  
550 infected with 16 different bacteria and monitored by live-imaging. The percentages of bright  
551 nuclei were used to derive kinetics plots (a) and the corresponding Area Under the Curves

552 (AUC) (b). Each point in the kinetics plots correspond to the means of triplicates and AUC  
553 histograms represent the means of the AUCs obtained for the kinetics of each replicate. Error  
554 bars represent the standard deviation (n=3). Stars indicate statistically significant differences  
555 between strains of the same species and NS a non-significant difference (one-way ANOVA, P  
556 < 0.05). Each of Tthe kinetics plot replicatess obtained with different bacterial species  
557 inducing “bright nuclei” were fitted with sigmoid model curves and the inflection point and  
558 curve steepness were calculated and represented as XY pairs (c). Means and standard  
559 deviations are represented.  
560

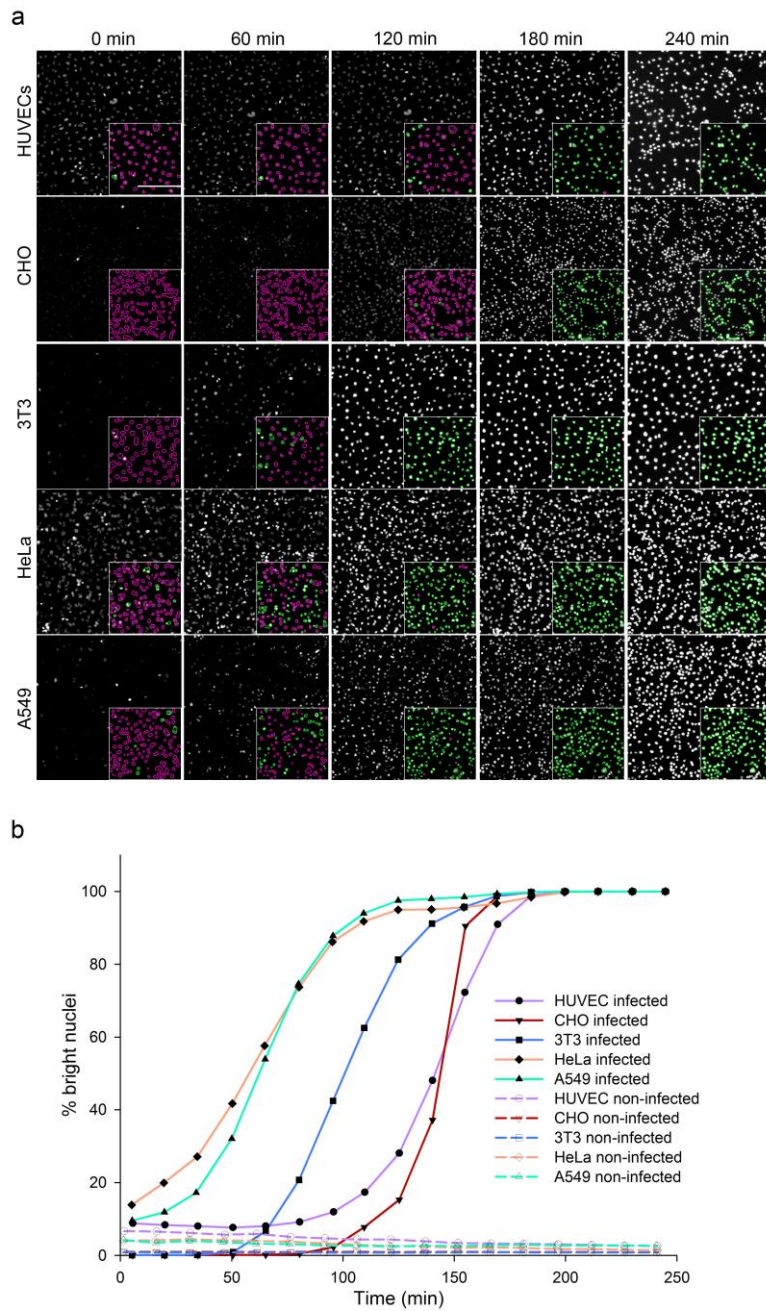
561 Figure 1



562

563

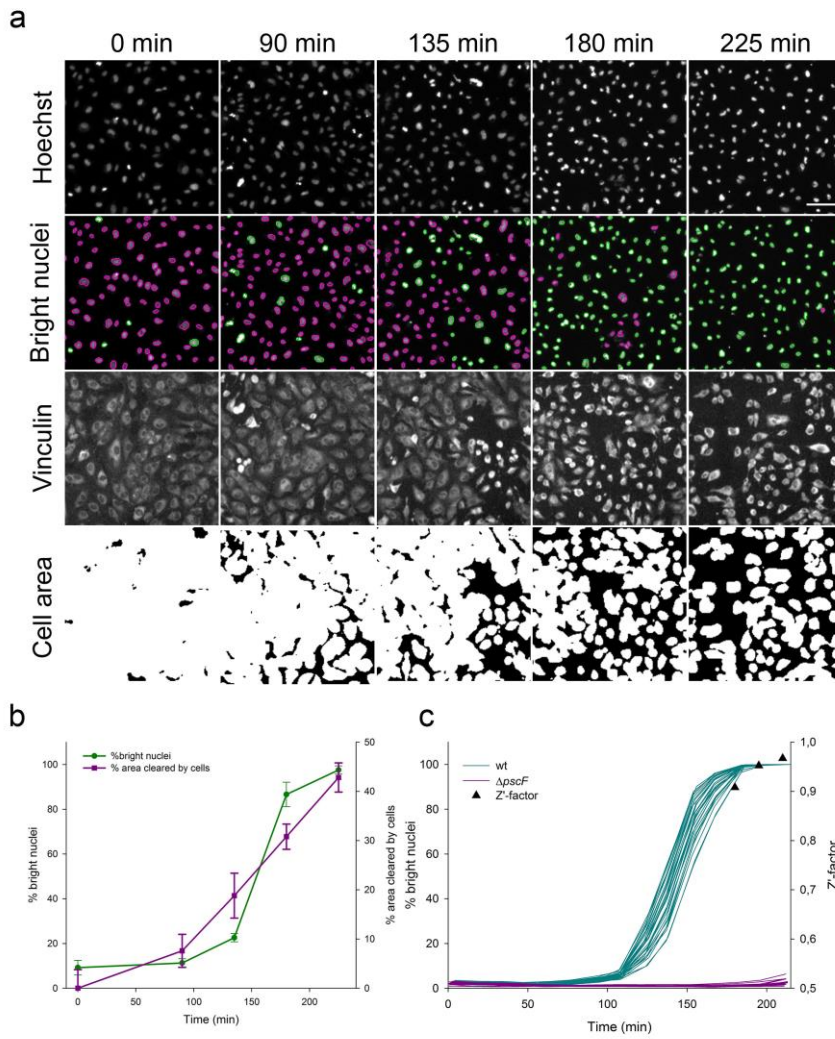
564 Figure 2



565

566

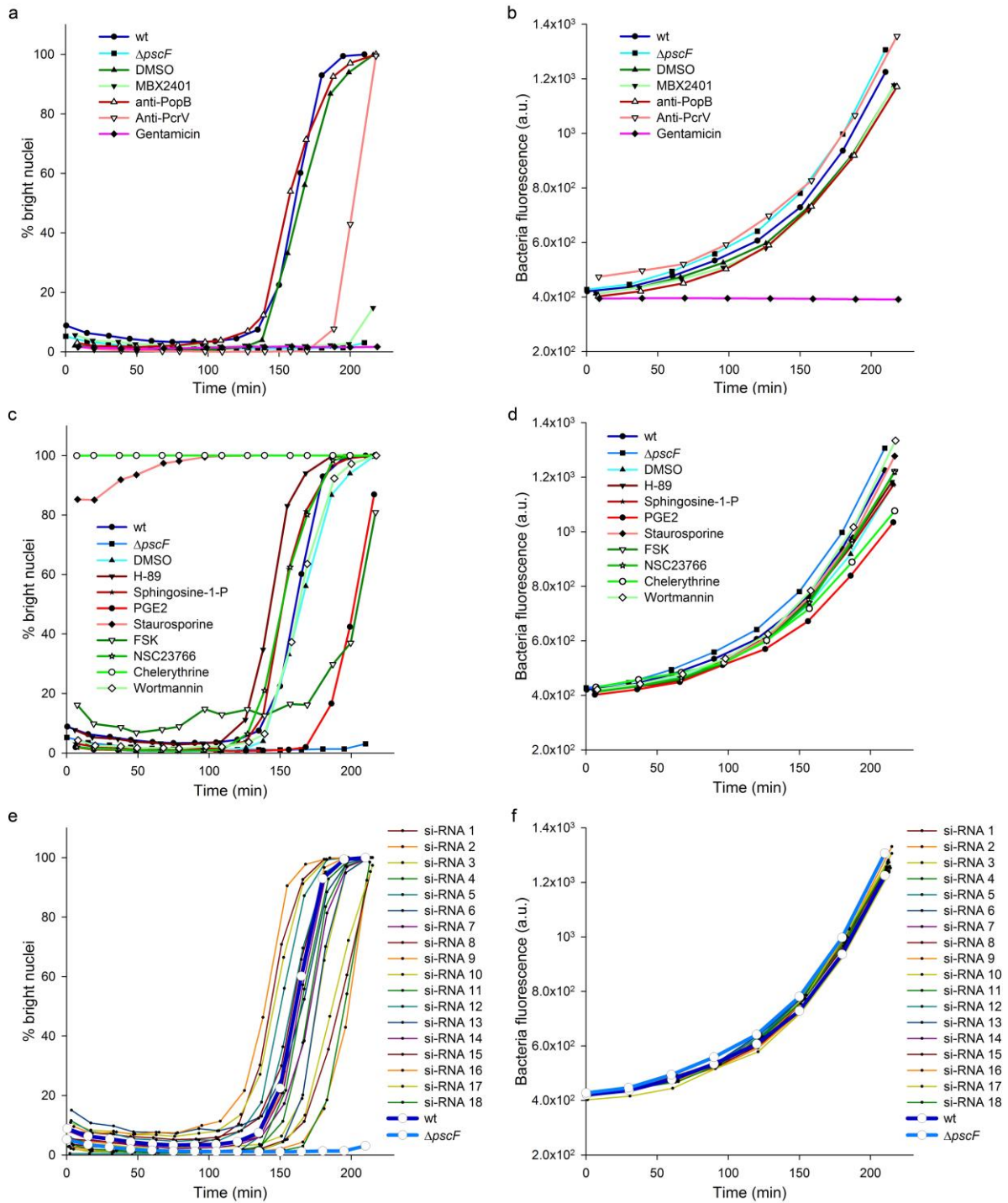
567 Figure 3



568

569

570 Figure 4

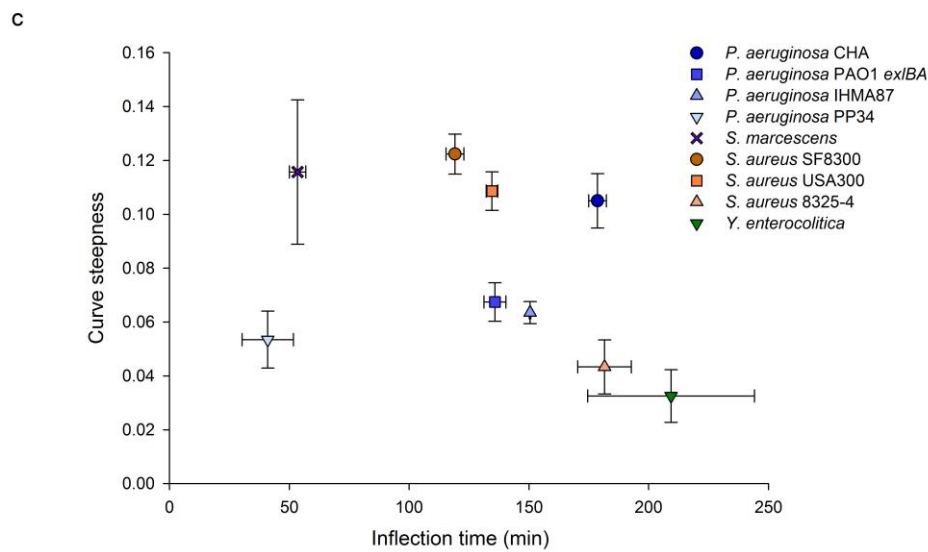
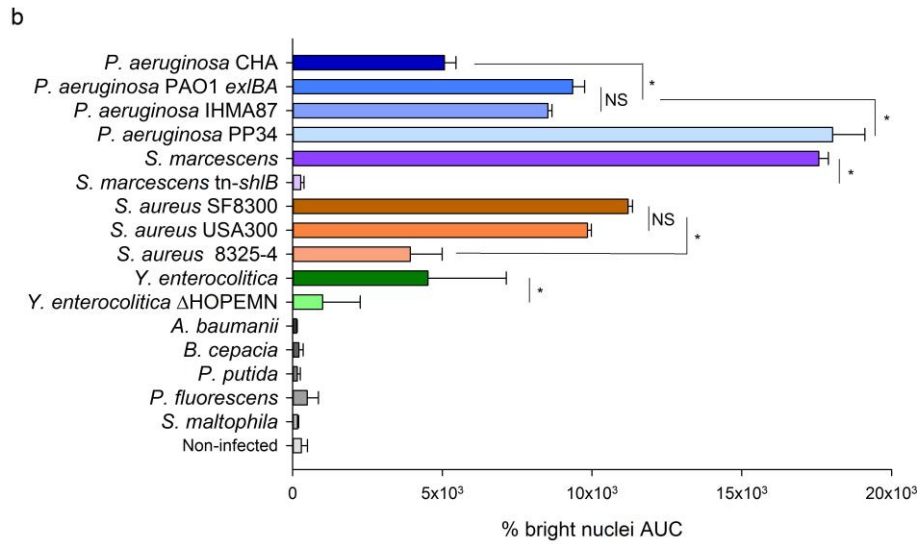
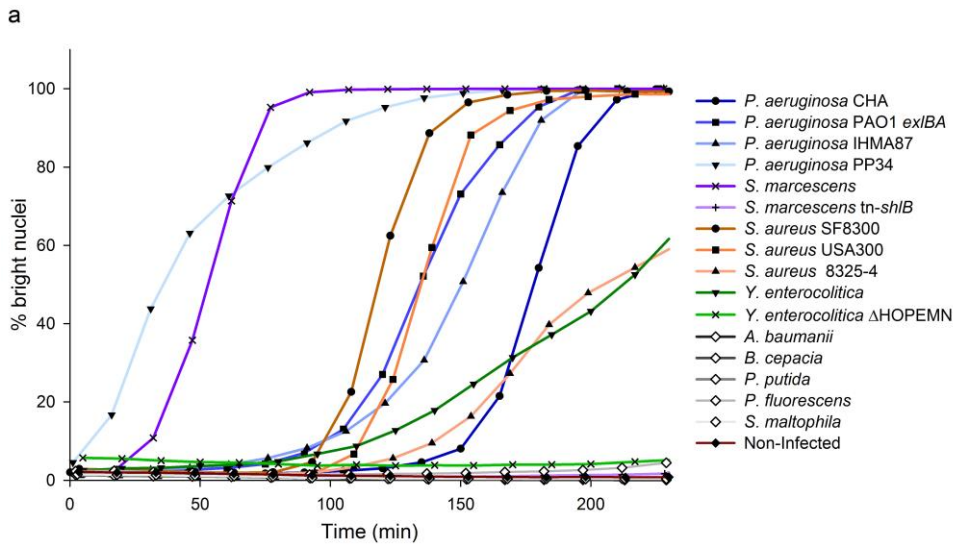


571

572

573 Figure 5

574



575